Acta Materialia 286 (2025) 120743

Contents lists available at ScienceDirect

Acta Materialia

journal homepage: www.elsevier.com/locate/actamat

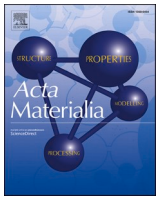

Full length article

Thermal spin-torque heat-assisted magnetic recording

S. Isogami [a,*], Y. Sasaki [a], Y. Fan [b], Y. Kubota [b], J. Gadbois [b], K. Hono [a], Y.K. Takahashi [a]

[a] Center for Magnetic and Spintronic Materials, National Institute for Materials Science (NIMS), Tsukuba 305-0047, Japan
[b] Seagate Technology, Recording Media Organization, Fremont, CA 94538, USA

ARTICLE INFO

Keywords:
Magnetic recording
Spin torque
Heat assisted
Antiferromagnet

ABSTRACT

To achieve higher recording density with lower power consumption than the current heat-assisted magnetic recording (HAMR) for next-generation, a more efficient writing with less laser power would be indispensable. An advanced HAMR concept is developed to address such specification, and the write ability has been demonstrated in multilayer media stacks comprising the core structures of antiferromagnetic MnPt and ferromagnetic FePt layers with the magnetic easy axis oriented perpendicular to the film plane. The concept is based on two distinct switching mechanisms: thermally activated (TA) and spin-transfer-torque (STT) assisted magnetization switching. The latter is driven by an out-of-plane temperature gradient (ΔT) in the MnPt/FePt multilayer which is referred as thermal spin-torque (TST) HAMR media. Pump-probe measurements reveal significant magnetic coercivity (H_c) modulation by ΔT at the local magnetization of the FePt layer. The hybrid mechanism with TA and STT can be separated by sweeping the delay time between the pump and probe laser pulses, and it is found that the STT dominates the mechanism for H_c modulation in the short delay time regime. Furthermore, the modulation of H_c of the FePt layer is demonstrated to be dependent on the magnitude and the direction of steady state ΔT. These results suggest that lower laser power consumption is achievable owing to the contribution of STT assisted switching in the TST-HAMR media.

1. Magnetic recording with high density and low power

The total amount of data generated from various applications has been exponentially increasing for years, thanks to the breakout of digital transformation technologies. The hard-disk-drives (HDDs) community has put tremendous efforts to develop revolutionary recording technologies to break records of recording density, providing cost efficient solutions to large volume data storage. Many research and developments have been extensively performed, for example, the material engineering of granular media [1–3] was initialized to reduce the grain diameter to increase the recording areal density [4]. The shrinking size of media grains inevitably leads to a decrease in the thermal stability, which is governed by the formula of $\frac{K_u V}{k_B T}$, where K_u is the uniaxial magneto-crystalline anisotropy constant, V is the volume of a grain, k_B is the Boltzmann constant, and T is the temperature. To overcome such issue, $L1_0$-ordered FePt granular media has been developed, which achieved a sufficiently high K_u value up to 7 MJ/m^3 [5,6]. However, this possesses significant challenge to the conventional magnetic writer to switch FePt grains as the magnetic coercivity (H_c) of granular media increases with K_u. This is referred as *trilemma in HDDs*.

Heat-assisted magnetic recording (HAMR) has been developed as a breakthrough technology to solve the trilemma problem [4–6]. To achieve both high thermal stability and write ability in the FePt granular media, laser pulses from writing heads are irradiated right before the moment of writing. The laser pulse raises the temperature of FePt grains to a level above the Curie temperature (T_c), which significantly reduces the switching barrier, enabling the writing with minimal magnetic fields required. Followed by locally field cooling the grains, the high thermal stability resumes, which stores information into FePt media. Therefore, the trilemma problem is solved by utilizing thermal energy to assist switching. And HAMR based HDDs have been shipped to data centers with a 28 TB capacity per drive in 2024. In addition, new technology such as multi-level recording in HAMR has been demonstrated to further increase data capacity in the future [7].

Besides of further increasing recording density, it is desirable to reduce the power consumption to heat FePt grains of the media, which is one of the important factors to be considered for large volume data centers. Here, we focus on utilizing the temperature gradient (ΔT), that is inevitably formed in the HAMR media by the heating of laser pulses, as a driving force of the magnetization switching in addition to the

* Corresponding author.
E-mail address: isogami.shinji@nims.go.jp (S. Isogami).

https://doi.org/10.1016/j.actamat.2025.120743
Received 29 August 2024; Received in revised form 3 January 2025; Accepted 12 January 2025
Available online 13 January 2025

conventional thermally activated (TA) switching. The spin-current, generated by the out-of-plane ΔT originating from the spin Seebeck effect (SSE) [8], would provide the magnetization of FePt grains with spin-transfer torques (STTs) to assist switching, therefore, it is expected that the laser power for the TA switching could be reduced. This is the new concept of magnetic recording based on the hybrid effect of STT and TA, leading to an advanced thermal spin-torque (TST)-HAMR media in the future.

In this study, we use the VN/MnPt/FePt multilayer structures to demonstrate the hybrid effects on the write ability in the FePt layer through the measurement of H_c. The H_c dependence on the out-of-plane dynamic ΔT induced by laser pulses is obtained for the sample. Two origins of STT and TA are separated via pump-probe measurements with the dynamical heating and cooling impacts resolved in the picosecond regime. The time-resolved cross-sectional ΔT is simulated to show the dynamical heat transfer in the samples. Further studies on H_c dependence on the steady state ΔT for the samples with and without MnPt layer indicate that the MnPt layer plays a crucial role for efficient recording to generate STT driven by ΔT.

2. TST-HAMR concepts

The HAMR with hybrid mechanisms of STT and TA, referred to as a TST-HAMR, could achieve both ultra-high efficiency and low power consumption. Figure 1(a) illustrates the principles of TST-HAMR, as compared to the current HAMR. Laser irradiation induces ΔT along the out-of-plane direction. With spin current generated from the antiferromagnets (AFMs) such as the MnPt layer under the FePt layer, the more efficient magnetization switching could be expected owing to the ΔT-driven STT, arising from the SSE [8]. For example, the spin momentum (σ) with $-z$ orientation that is represented by the green allows with balls, originating from the possible uncompensated magnetic moment at the AFM/FePt interface ($M_{\mathrm{Mn}}^{\mathrm{UC.}}$), could assist the magnetization switching of the FePt layer from up-to-down (details are discussed at the Section 4.4), while it is not expected for the conventional system without AFM layer. Figure 1(b) depicts the energy diagram showing the bi-stable magnetic states of the FePt layer separated by an energy barrier of K_uV. The energy barrier can be suppressed by TA with uniform heating, in addition, the STT can serve as an extra driving force for magnetization switching. Figure 1(c) illustrates the expected hysteresis loops impacts from the TA and the STT. The TA is responsible for both H_c reduction and demagnetization, while STT primarily contributes to only H_c reduction, because the SSE induced spin-angular momentum transfer can occur without charge transfer, resulting in no Joule heating or extra power consumption. Thus, demagnetization caused by elevating temperature is unrelated with STT.

Heavy metals such as Pt are the representative spin sources utilizing spin Hall effect to generate STT to the adjacent ferromagnetic layer. However, it has been proposed that AFMs have a potential to achieve more efficient spin generation driven by the ΔT [9–12]. We focus on the MnPt as a candidate of AFMs for the following reasons: first, the same atomic order with $L1_0$ and lattice constants as the FePt; second, the extremely high Néel temperature reaching 970 K [13]. These characteristics allow us to prepare the full epitaxial multilayer samples, and the AFM phase is stable regardless of the representative working temperature by laser pulses of HAMR media around 700 K. Figure 1(d) shows the crystal structure of $L1_0$-MnPt, in which the stable magnetic structure with collinear AFM is indicated by arrows. Although two possible collinear magnetic structures of MnPt were reported, with Néel vectors pointing in out-of-plane and in-plane directions [13,14], the Néel vector is determined to be parallel to the out of-plane direction in the present MnPt layer by controlling its atomic composition, as revealed by the enhanced H_c of the top FePt layer (see Fig. S1 in the supplemental material).

3. Experimental techniques

3.1. Thin film growth and microfabrication

MgO substrates are cleaned by ultrasonic with ethanol and acetone, followed by *in-situ* thermal flashing at 450 °C performed in the magnetron sputtering chamber. Base pressure of the chamber is kept being 5×10^{-7} Pa. The VN film is deposited at 320 °C via nitrogen reactive sputtering with the DC input power of 30 W, of which the gas flow ratio of N to Ar is set to be 50 % with the pressure of 1 Pa. The MnPt and FePt films are deposited at 420 °C and 450 °C, respectively, with the Ar gas pressure of 1 Pa and the DC input power of 30 W. 2-nm-thick MgO capping layer is deposited at room temperature (RT) to prevent surface oxidation on the FePt layer. Microfabrication is performed using photolithography and Ar ion milling to form the Hall-bar devices shown in Fig. S4 in the supplemental material. Magnetic hysteresis loops are measured using a magnetic properties measurement system (MPMS) at RT.

3.2. TEM observation

TEM samples for the cross-sectional microstructure measurements are prepared by a focused ion beam lift-out technique (FEI Helios Nanolab 650). To avoid damage during the milling, Ni film is deposited on the film surface. TEM observation is carried out using a Titan G2 80–200 with a probe aberration corrector. Energy-dispersive X-ray spectroscopy (EDS) is conducted using an FEI Super-X EDX detector.

3.3. MOKE measurements via pump-probe method

Spin re-orientation by the laser pulse irradiation is investigated using a pump-probe method with an ultrafast pulse laser system, Yb:KGW laser source, of which the center wave length is 1028 nm, the pulse duration is 290 fs, and the repetition rate is 10 kHz. The pump power is varied from 0 to 60 mW with the spot diameter of ~0.1 mm. The power can be described as pomp fluence ranging from 0 to 760 J/m^2. The wavelength of probe pulses is converted to 514 nm by BBO crystal. The probe pulses are linearly polarized by a polarizer with the power below 100 μW. The transient probe polarization owing to the transient magnetic state is detected by the balanced detection technique with a half-wave plate and Wollaston prism. Magneto-optical Kerr effect (MOKE) is measured by sweeping the magnetic field along the direction of 25° with respect to the film normal, to investigate spin re-orientation process of the FePt layer under various delay time (Δt) between pump and probe pulses.

4. Results and discussion

4.1. Film characterization by cross-sectional TEM

Fig. 2(a) illustrates the film stacking structure in this study. The VN layer is deposited on the MgO substrate to improve the interfacial roughness. The stacking structure is confirmed by the cross-sectional high-angle annular dark-field scanning transmission electron microscopy (HAADF-STEM) image shown in Fig. 2(b). Fig. 2(c1) and 2(c2) show the nano-beam diffraction (NBD) patterns for the MnPt and FePt layers, respectively. The NBD patterns arise from the (001) superlattice, indicating the $L1_0$-atomic-order as depicted by the unit-cell [Fig. 1(a)] for both MnPt and FePt layers. Fig. 2(d1)−2(d5) show the energy dispersive spectroscopy (EDS) mapping, suggesting no interdiffusion and/or alloying at interfaces (see Fig. S2 in the supplemental material for the line profiles). It is worth to pointing out that the stripe pattern can be seen in the mapping images of Fe, Mn, and Pt in the atomic resolved EDS image of Fig. 2(e), confirming the atomic $L1_0$-order of MnPt and FePt layers. These results prove the high quality epitaxial growth of the present multilayer samples.

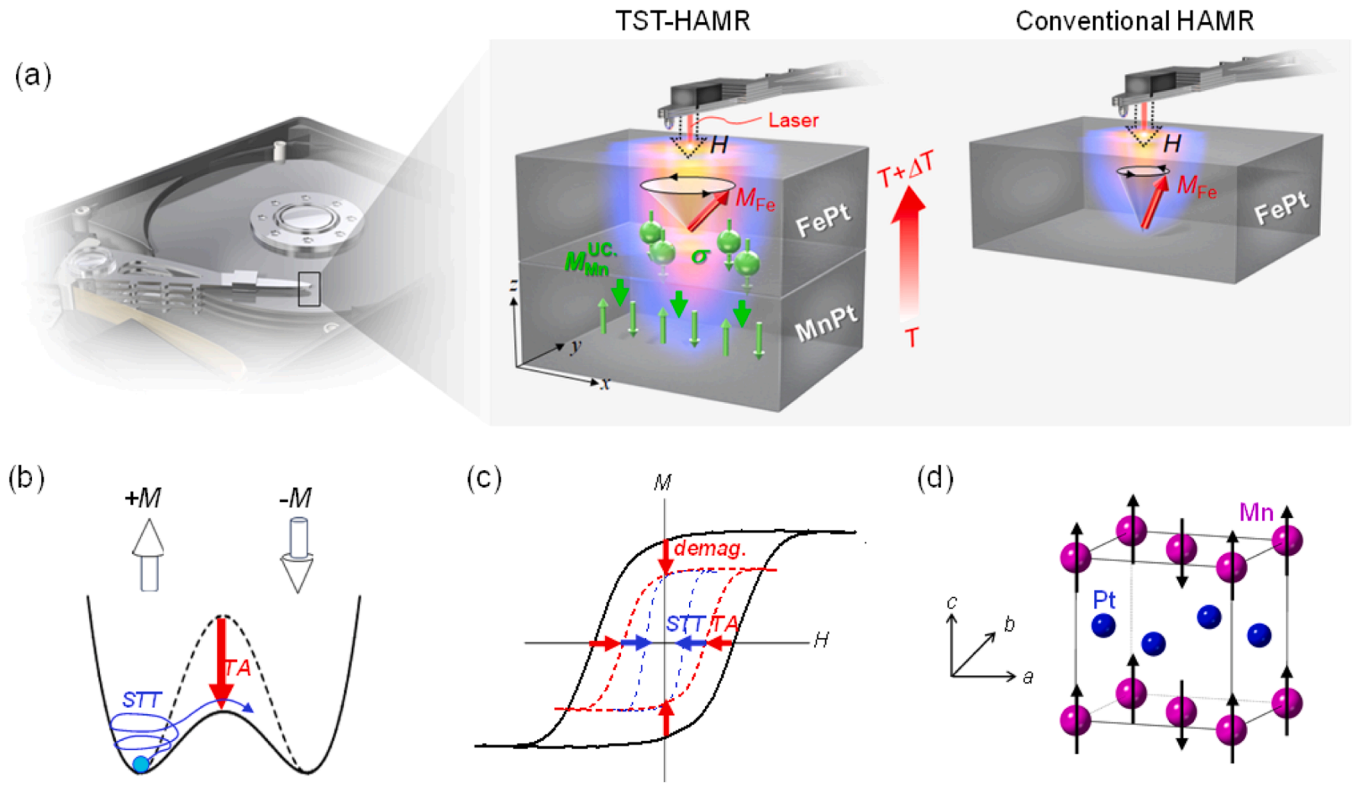

Fig. 1. (a) Concept of the thermal spin-torque heat-assisted magnetic recording (TST-MAHR) with the $L1_0$-MnPt / $L1_0$-FePt bilayer system, together with the conventional HAMR. The thick green arrows at the MnPt/FePt interface represent the uncompensated Mn moment ($M^{UC.}_{Mn}$) induced by the exchange magnetic interaction between Mn and Fe. The green arrows with balls represent the spin angular momentum (σ) that is parallel to the $M^{UC.}_{Mn}$. The writing field (H) from the HDD-head is shown by dashed arrow. (b) Energy diagram showing the bi-stable magnetic states of FePt and its change depending on the heating by laser pulses. (c) Possible magnetic hysteresis loops of the FePt layer with temperature gradient by laser pulses. (d) Schematic illustration of $L1_0$-MnPt unit cell together with collinear antiferromagnetic structure.

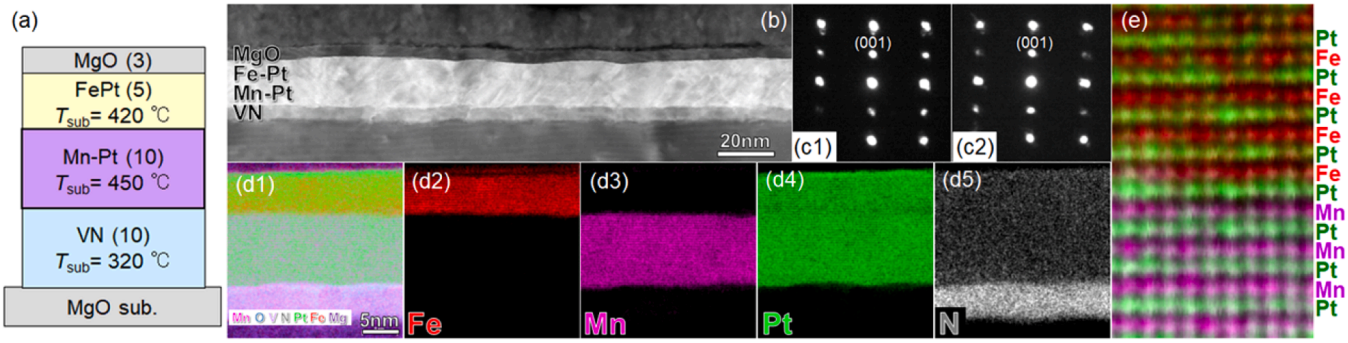

Fig. 2. (a) Representative stacking structure for the TST-HAMR media. (b) Cross-sectional high-angle annular dark-field scanning transmission electron microscopy (HAADF-STEM) image. (c) Nano-beam diffraction (NBD) patterns for the MnPt (c1) and FePt (c2) layers. (d) Energy dispersive spectroscopy (EDS) mappings for each element. (e) Atomic-resolved EDS image at the MnPt/FePt interface.

4.2. H_c modulation by laser pulses

To investigate the local magnetization switching efficiency of the FePt layer, we measure the demagnetization and H_c from the MOKE hysteresis loops via pump-probe method [Fig. 3(a)] using the sample of MgO substrate // VN(10 nm) / MnPt(10 nm) / FePt(10 nm) / MgO(2 nm). This method allows us to investigate spin re-orientation process in the FePt layer by varying Δt and pump power (F_p), in which the repeated dynamic heating and cooling cycles are resolved in pico-seconds time scale [15–18].

We verify that the MOKE hysteresis loop without pump pulse (black symbols) agrees with the magnetic hysteresis behavior measured using MPMS [see Fig. S1(b) in the supplemental material]. This confirms that the intensity of probe laser pulses is low enough to avoid thermal activation of the sample. In contrast, the loops are dramatically impacted by pump pulses, showing dependence on the Δt: similar signal with remarkably small H_c at Δt =–1 ps (red symbols), and remarkably small MOKE signal with large H_c at Δt = +1 ps (blue symbols), followed by the increase of MOKE signal with the decrease of H_c obtained at Δt = +30 ps (green symbols). Figure 3(b) shows the demagnetization dependence on Δt, which is determined by the ratio of MOKE signal obtained at each Δt to the value measured without pump laser. The magnetization is governed by temperature in general, so that Fig. 3(b) indicates the elevated temperature in the FePt layer. The magnetization decreases by ~75 % of

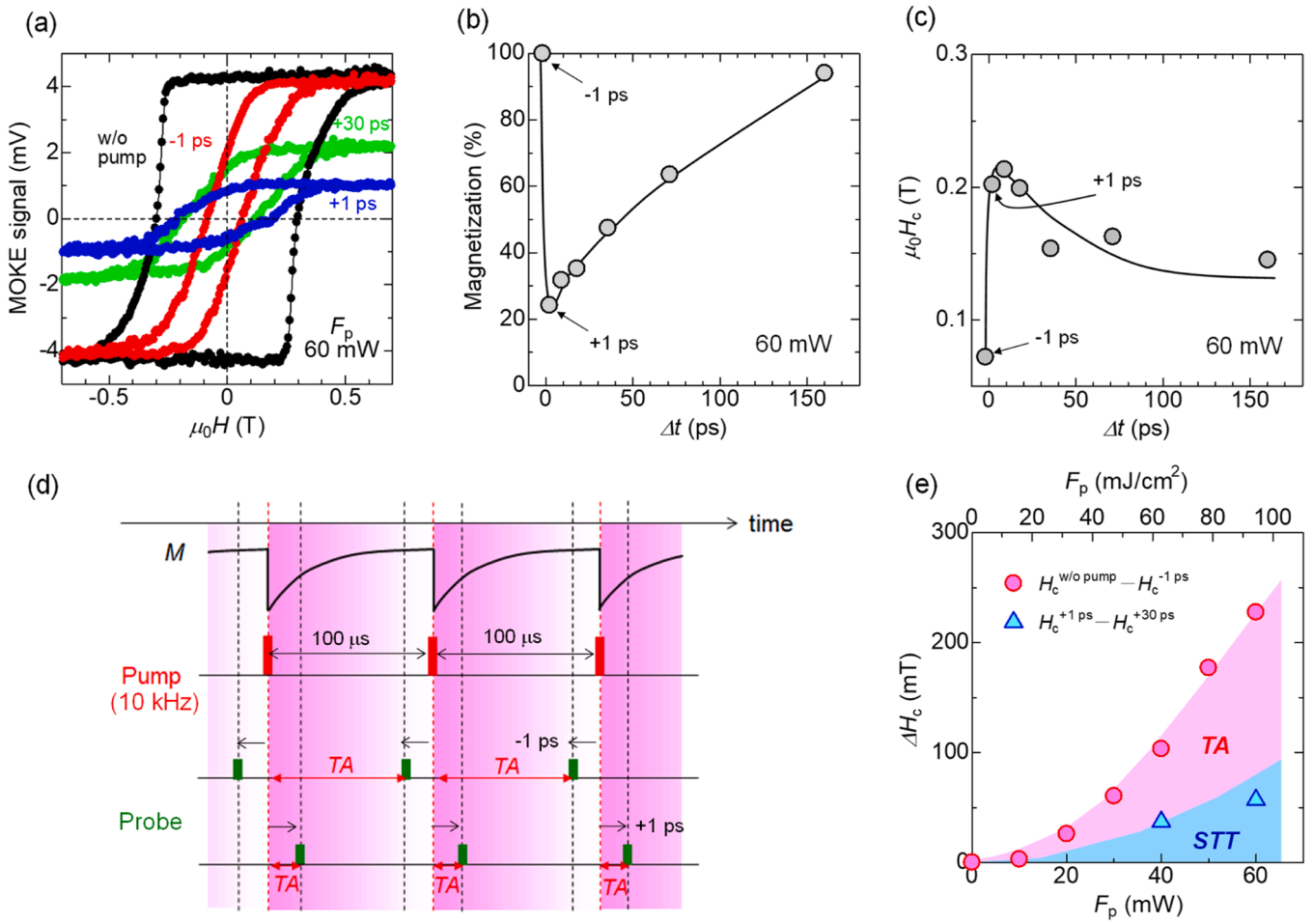

Fig. 3. (a) Magneto optical Kerr effect (MOKE) as a function of magnetic field (H) measured via pomp-probe method with different delay time (Δt) for the multilayer sample, MgO substrate//VN(10 nm)/MnPt(10 nm)/FePt(10 nm). (b,c) Demagnetization (b) and magnetic coercivity (H_c) (c) as a function of Δt. The solid lines are guides to the eyes. (d) Schematic illustration of pump-probe measurements in this study with 10 kHz, where M represents the magnetization as shown in Fig. 3(b), and TA with arrows corresponds to the entire thermal activation energy. Note that the MOKE signal probed at the delay time of −1 ps includes large amount of TA contribution. (e) H_c difference (ΔH_c) as a function of pump power (F_p), in which the ΔH_c for w/o pump and Δt =−1 ps (red circle) as well as Δt = +1 ps and +30 ps (blue tringle) correspond to the contributions from TA and STT, respectively.

initial value at Δt = +1 ps, suggesting the highest temperature in the FePt layer induced by the pump laser pulse heating. Then the magnetization starts recovery to the initial magnitude with Δt, suggesting heat dissipation from the FePt layer. It is inferred from the measurement that the magnitude of magnetization is fully recovered before the irradiation of next pump pulse, consistent with the expectation that the period of pump pulse of 100 μs (the pulse repetition in this setup is 10 kHz) is long enough to cool down the temperature of FePt layer to the RT.

Figure 3(c) plots the evolution of H_c with Δt, determined from the MOKE hysteresis loops in Fig. 3(a). The largest H_c is observed at Δt = +1 ps, followed by a decrease with time. The sudden increase of H_c from Δt of−1 to +1 ps indicates the local magnetization, influenced by the pump laser beam, is flipped to the magnetic state of surrounding FePt (depicted by the dark loop in Fig. 3(a)). The pump pulse instantly reduces the local magnetocrystalline anisotropy. The surrounding hard FePt switches the relatively soft magnetization via exchange coupling. As the temperature cools down, the magnetocrystalline anisotropy recovers. This is expected to increase the energy barrier to prevent the local magnetization from switching away from the magnetic state of surrounding FePt. However, such switching process occurs at Δt = +1 ps and continues beyond 160 ps, when the external magnetic field is applied opposite to the direction of FePt magnetization. It is revealed by the H_c reduction in Fig. 3(c) and implies that the H_c reduction is influenced by the time integration of the temperature, i.e., the energy of TA, rather than the actual temperature at specific Δt. The minimum of H_c observed at Δt =−1 ps is due to the maximum of time integrated TA. Figure 3(d) illustrates the time-resolved pulse irradiation and magnetization to depict the influences from the different magnitude of TA. The demagnetization occurs at the pump pulses irradiated once every 100 μs. For the probe pulse with Δt = +1 ps, although the temperature is high, TA may be small due to the significantly short integration time of 1 ps. Conversely, for the probe pulse at Δt =−1 ps, although the heat dissipation is almost completed and the actual temperature returns to RT, TA can be sufficiently large due to the long period of approximate 100 μs, as indicated by red arrows.

Moreover, Fig. 3(c) shows the decrease of H_c exhibiting two significantly different stages: (i) a rapid drop within +30 ps and (ii) a much slower reduction beyond +30 ps. The fast drop of H_c in the stage (i) suggests the local magnetization may experience a torque which assists the switching quickly, while the time integrated TA dominates the slow H_c change in the stage (ii). Figure 3(e) shows the pump-laser-power induced total change of H_c with respect to no pump power applied together with the H_c change from Δt of +1 to +30 ps. The origin of H_c change from Δt of +1 to +30 ps is likely to be STT driven by the vertical temperature difference induced by pump laser pulse, which will be further investigated in the following analysis and experiments.

4.3. Heat transfer simulation with laser pulses

To estimate the time-dependent ΔT along the in-plane and out-of-plane in the multilayer sample, the time-domain cross-sectional heat transfer with the ultrashort pulse laser is simulated as shown in Figs. 4 (e1)−4(e3). We use the COMSOL multi-physics package [19], in which we set laser source with a pulse duration of 290 fs and a repetition frequency of 10 kHz. Gaussian distribution is applied to the laser power, which is irradiated at the surface of MgO capping layer. The initial temperature is 300 K. The dynamical temperature is simulated from 0 to 150 ps with the time step of 0.1 ps. Parameters, such as thermal conductivity for each layer etc., are addressed in Fig. S3 in the supplemental material.

Following one pulse irradiation, the temperature of the FePt layer increases rapidly, reaching over 700 K within +1 ps. Such temperature is found to be relatively higher than the value indicated in the previous report [20]. This discrepancy may be caused by errors in the input parameter of laser power density to the model, because the spot size and/or Gaussian distribution are not precisely measured. Nevertheless, the model reveals the heat transfer as well as the ΔT in each layer, which allows the impacts from TA and STT to be understood individually. The model indicates that FePt experiences a remarkably high temperature at $\Delta t = +1$ ps, which is consistent with the experimental result of maximum demagnetization at $\Delta t = +1$ ps [Fig. 3(b)]. The cooling process starts after $\Delta t = +2$ ps in the FePt layer, as the heat is transferred into the MnPt and VN layers [Figs. 4(a2) and 4(a3)]. Figure 4(b) indicates the temperature difference in the 10-nm-thick FePt and MnPt layers (ΔT_{FePt} and ΔT_{MnPt}) as a function of Δt. The ΔT_{FePt} drastically decreases at $\Delta t = +2$ ps, while the ΔT_{MnPt} shows a maximum value up to ~34 K, then it gradually decays. The simulation results suggest that ΔT_{MnPt} remains in the delayed time regime up to approximate +20 ps. The ΔT_{MnPt} could introduce SSE to drive spins into FePt layer. This effectively induces a torque assisting to switch the magnetization, thus reducing the H_c. Therefore, the rapid decrease of H_c observed in the Δt regime of +1 to +30 ps in the experiments [Fig. 3(c)] might be predominantly originated from the STT contribution in addition to the TA, which must be regarded as a STT-assisted HAMR. As Δt increases beyond +30 ps, the STT contribution vanishes due to the decay of ΔT_{MnPt} resulting from heat dissipation. The TA dominates the following H_c reduction via the time integration effect of residual heat (see Fig. S3 in the supplemental material for much longer Δt). Thus, the H_c shows the minimum at $\Delta t = +1$ ps.

4.4. H_c modulation by static thermal gradient and possible mechanism

To reveal the dominant spin source driven by ΔT, and to demonstrate the H_c dependence on the direction of ΔT which is not possible for the pump-probe method, it is desirable to study magnetization reversal behavior with controlled steady state temperature gradients applied vertical to the sample.

Figure 5(a) shows the anomalous-Hall hysteresis loops at different temperatures (without ΔT) for the same sample of MgO substrate // VN (10 nm) / MnPt(10 nm) / FePt(10 nm) / MgO(2 nm). ρ_{xy} in the vertical axis represents the transverse resistivity, of which measurement configuration is depicted by the inset in Fig. 5(a). The temperature is set to be $T_1 = T_2 = 300$ K, 400 K, and 500 K, where T_1 and T_2 respectively represent the temperature measured by the thermocouples placed near the sample stage (back side of the sample) and the on-chip heater (front side of the sample), since it is technically impossible to measure the actual temperature directly from the top and bottom surfaces of the layer with only 10-nm thickness (see Fig. S4 in the supplemental material for detailed setups). The H_c is measured to be 0.31 T for 300 K, while 0.25 T for 400 K and 0.18 T for 500 K. The H_c reduction with increasing temperature can be attributed to the reduction of magnetization switching barrier by TA as depicted in Fig. 1(b).

The measurement system allows for either positive or negative temperature gradient depending on the temperature control of T_1 and T_2 as shown in Fig. S4 in the supplemental material. Once steady state ΔT ($\Delta T = T_2 - T_1$) is applied, it is evident that the H_c decreases for $\Delta T > 0$, which is consistent with the results of the pump-probe measurements as shown in Fig. 3. Conversely, the H_c shows increment for $\Delta T < 0$, i.e., the opposite temperature gradient. Figure 5(c) shows the dependence of H_c, normalized by the value at $\Delta T = 0$ for each T_1. A linear relationship is observed between H_c and ΔT, consistent with the expectation of SSE that the induced spin transferring density increases with the temperature

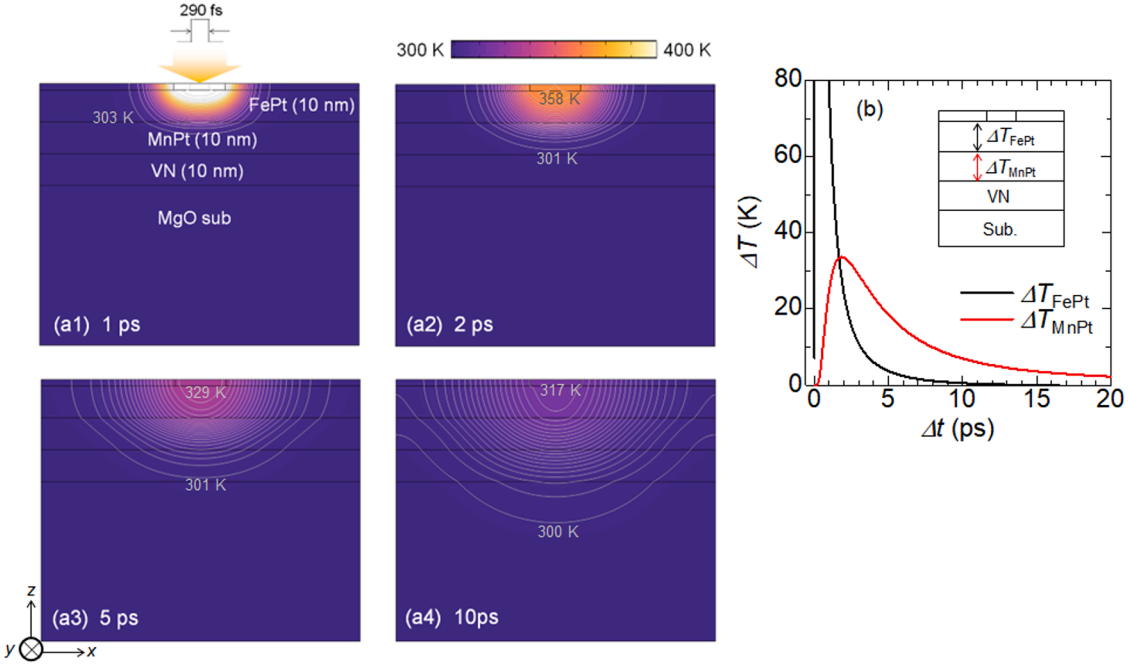

Fig. 4. (a1-a4) 2D heat transfer simulation for the multilayer sample, MgO substrate//VN(10 nm)/MnPt(10 nm)/FePt(10 nm) with $\Delta t = 1$ ps, 2 ps, 5 ps and 5 ps, where parameters such as thermal conductivity are described in the supplemental material. (b) Out-of-plane temperature difference in the 10-nm-thick FePt (ΔT_{FePt}) and MnPt (ΔT_{MnPt}) layers as a function of Δt.

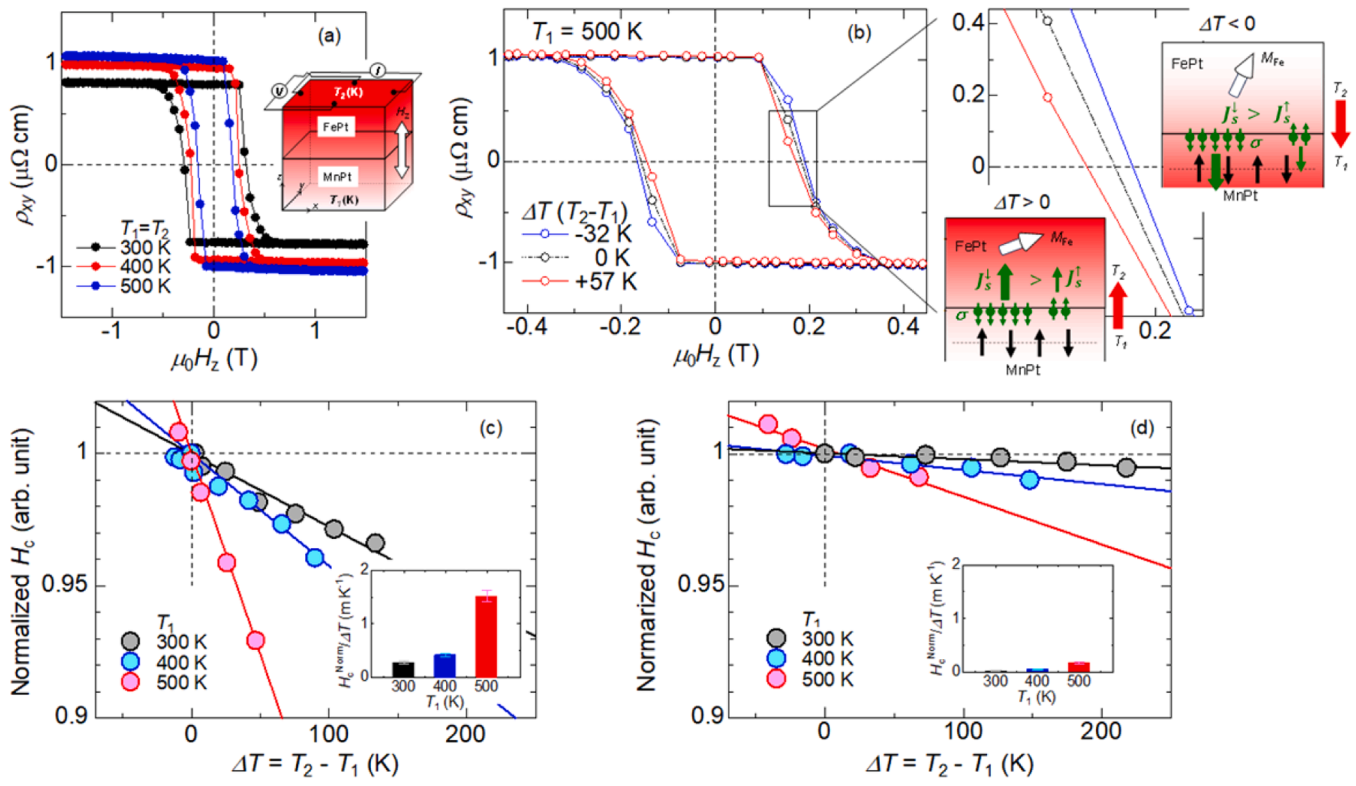

Fig. 5. (a) Transverse Hall resistivity (ρ_{xy}) as a function of out-of-plane magnetic field (H_z) under the heating of $T_1 = T_2 = 300$ K, 400 K, and 500 K for the multilayer sample, MgO substrate//VN(10 nm)/MnPt(10 nm)/FePt(10 nm). (b) Same measurements as Fig. 5(a), but with the temperature gradient (ΔT), which corresponds to the temperature measured by thermocouples those are placed at top (T_2) and bottom (T_1) sides of the samples. The magnified image corresponding to the loop surrounded by square is shown in right hand figure. Two schematic illustrations show the possible STT phenomena for positive and negative each ΔT. σ represents the polarized spin of $M_{Mn}^{UC.}$. (c) Normalized magnetic coercivity (H_c) depending on $\Delta T = T_2 - T_1$. The insets represent the normalized H_c value per ΔT, which is based on the slope of linear fitting lines. (d) Same as Fig. 3(c), but for the control sample without MnPt layer.

difference linearly. And the sensitivity of H_c dependence on ΔT is pronounced at higher T_1, as also shown in the bar graph of the inset. To provide further insights into the spins driven by ΔT in the MnPt layer, we perform the control experiments in the sample without MnPt layer, MgO substrate // VN(10 nm) / FePt(10 nm) / MgO(2 nm), with results shown in Fig. 5(d). It is noted that the H_c reduction is remarkably small in the control sample without MnPt, suggesting the major (minor) role in the MnPt (FePt) layer for H_c reduction by ΔT. Furthermore, the magnetic properties of FePt layers with and without MnPt are shown in Fig. S5 in the supplemental material, indicating the similar magnetic properties between samples. These results lead us to conclude that the MnPt could be a pronounced spin source and must be responsible for the significant H_c modulation driven by ΔT, comparing to the FePt layer itself.

According to the results shown in Fig. 3(e), determined from the H_c evolution in pump-probe measurements, significant STT component was revealed, which was estimated to be ~35 % of total H_c reduction at 60 mW pump power. On the other hand, the previous work suggests the relatively small contribution of thermal STT in the metallic spin-valves, which exerts a ~1 % tilting of the in-plane magnetization of the CoFeB layer [21]. We attribute the large STT in the present stack to three reasons. (i) The spin-transfer efficiency is enhanced at the heterojunction interface of MnPt/FePt. The coherent epitaxial growth of the FePt layer is realized on the MnPt layer, as revealed in Fig. 2(e). The spin-transfer efficiency at the interface is related to the spin-mixing conductance, which is governed by the interfacial crystal structure and electronic band structure [22,23]. Moreover, there exists no spacer layer between FePt and MnPt to introduce spin relaxation process. The larger STT would be expected in the present stack than the sample with amorphous CoFeB and spacer layers of 10–100 nm as reported in [Ref. 21]. (ii) The high pump laser pulse energy is utilized in the present experiments and is swept up to 760 J/m^2, which induces a large temperature difference between the top and bottom of MnPt layer to drive the thermal spin current, while a pump pulse energy of 10.6 J/m^2 is deployed to the stack in [Ref. 21]. And (iii) the saturation magnetization (M_s) and the T_c of FePt (~1.1 T and ~700 K) are smaller than CoFeB (~1.5 T and ~900 K). The STT is inversely proportional to the M_s, so that a larger magnitude of thermal STT is expected as compared to the [21]. In addition, the pump laser directly heats the FePt layer while the CoFeB layer is heated after the 10–100 nm thick Cu spacer layer. Therefore, significant demagnetization can be realized in FePt, as compared to the CoFeB, resulting in enhanced thermal STT for the FePt layer.

Based on the results in Figs. 5(c) and 5(d), we find that the H_c modulation (i.e., expansion or contraction) can be attributed to the STT that is exerted from the MnPt layer, originating from the principles of SSE. It has been reported in the exchange coupled bilayer systems such as antiferromagnetic Mn-Ir/ferromagnet that the $M_{Mn}^{UC.}$ is induced at the interface as a result of magnetic coupling between Mn and ferromagnet, which has been revealed by the X-ray magnetic circular dichroism so far [24]. The coupling configuration depends on the ferromagnetic materials: parallel configuration in the case for Mn and Co, while antiparallel configuration for Mn and Fe as in this study [24]. Therefore, down (up) $M_{Mn}^{UC.}$ is possible at the MnPt/FePt interface when the magnetization of FePt layer is oriented in the up (down) direction, which suggests that the $M_{Mn}^{UC.}$ could behaves like a ferromagnetic sub-layer adjacent to the FePt layer with the net magnetization antiparallel to FePt. Considering the SSE in ferromagnets suggested by Hu *et al.* [25], the spin current with both up- and down-spin channels flow in the same/opposite direction, which is determined by the electronic band structure at the Fermi level. Although the band structure of $M_{Mn}^{UC.}$ is not clear, we assume here that

both spin channels flow in the same direction as the ordinary ferromagnet, in an attempt to explain the H_c change shown in Fig. 5(b) [25]. For $\Delta T > 0$ with the initial state of up-magnetization of Fe and down-direction of $M_{Mn}^{UC.}$, the spin current for the down-spin channel ($J_s^{\sigma_\downarrow}$) is greater than that for the $J_s^{\sigma_\uparrow}$ because the $\sigma_\downarrow$ corresponds to the majority spin channel for $M_{Mn}^{UC.}$. The net spin current ($J_s = J_s^{\sigma_\downarrow} + J_s^{\sigma_\uparrow}$) is dominated by the $J_s^{\sigma_\downarrow}$, which can exert the STT favorable from up to down for the magnetization of FePt, resulting in the reduction of H_c, as depicted by the left schematic illustration in Fig. 5(b). In the switching back from down to up, the majority spin channel of $M_{Mn}^{UC.}$ is changed from $\sigma_\downarrow$ to $\sigma_\uparrow$, resulting in the reduction of H_c as well. Therefore, H_c can be reduced at both sides of hysteresis loop. Conversely, for the reversed $\Delta T < 0$, which is opposite temperature gradient, the magnitude of J_s is still dominated by the $J_s^{\sigma_\downarrow}$. However, this J_s exerts the STT favorable from down to up for the magnetization of FePt because of the reversed direction of J_s. As a result, H_c is enhanced, as depicted by the right schematic illustration in Fig. 5(b). In the switching back from down to up, enhanced H_c is observed because the majority spin channel of $M_{Mn}^{UC.}$ is changed from $\sigma_\downarrow$ to $\sigma_\uparrow$. Therefore, both side of H_c can be enhanced.

Nevertheless, it is sure that the horizontal shift of the out-of-plane hysteresis loop, as reported in Refs. [26,27], can be attributed to the z-polarized spin injection by the in-plane charge current, which cannot expand or contract the H_c of the loop in principle. This is because the direction of z-polarized spin and the resultant STT are constant regardless of the magnetization switching. This phenomenon might be also applicable for the device with z-polarized spin injection by the SSE. However, as we explained above, the $M_{Mn}^{UC.}$ induced at the MnPt/FePt interface plays a role of z-polarized spin source, and its direction can be reversed following the FePt magnetization switching, which gives rise to the H_c modulation (i.e., expansion or contraction), not horizontal loop shift. This is the most unique points in the present TST-HAMR concept [Fig. 1(a)].

Questions remain regarding the mechanism of ΔT-driven J_s injection into the top FePt layer in the present bilayer structure. Some possible mechanisms have been reported so far, including the diffusion of spin polarized conduction electrons [28] and the magnons [29] driven by ΔT. In the reported case of Pt/AFM system with the AFM insulator of NiO, the interfacial temperature gradient across the surface normal induces a local J_s, which diffuses into the metallic Pt layer, as suggested by Isaiah *et al* [11]. In spite of the same AFM insulator, it was proposed that the induced phonons may drag magnons arising from the magnon-phonon interaction in the Pt/Cr_2O_3 system by Seki *et al* [9]. Although it is unclear whether these mechanisms can be similarly applied to our sample with metallic AFM of MnPt, and how the $M_{Mn}^{UC.}$ contributes to spin current driven by SSE, a careful demonstration using various AFM materials and/or a spin-resolved theoretical band calculation would be useful to promote the understanding of J_s injection mechanism in the HAMR systems.

5. Conclusion

The H_c reduction induced by the static and dynamical ΔT-driven STT and TA have been evaluated using epitaxial multilayer samples of MgO substrate // VN(10 nm) / MnPt(10 nm) / FePt(10 nm) / MgO(2 nm), to demonstrate the advanced TST-HAMR concept. The H_c of FePt layer clearly increases (decreases) for the static $\Delta T < 0$ ($\Delta T > 0$), while the effect is significantly suppressed by removing the MnPt antiferromagnetic layer. It indicates that the MnPt layer plays a significant role to reduce H_c by ΔT. Two origins of STT and TA are separated via pump-probe measurements with the dynamic heating and cooling impacts resolved in picosecond delayed time regime. Moreover, the dynamical heat transfer from the laser beam to the multilayer sample is simulated using the COMSOL multi-physics package. The results suggest that the FePt layer is instantly heated at $\Delta t = +1$ ps and then cooled after $\Delta t = +2$ ps. The MnPt layer experiences heating after $\Delta t = +2$ ps and the resulting ΔT lasts for approximate +20 ps, which can be the origin to generate STT. Both experimental and simulation results imply that STT is the predominant mechanism to reduce the H_c within +30 ps after the pump lase pulse irradiation, while TA dominates the H_c reduction when the STT vanishes at longer Δt.

CRediT authorship contribution statement

S. Isogami: Writing – original draft, Project administration, Methodology, Investigation, Data curation. **Y. Sasaki:** Writing – review & editing, Validation, Investigation, Data curation. **Y. Fan:** Writing – review & editing, Validation, Formal analysis, Conceptualization. **Y. Kubota:** Validation, Methodology. **J. Gadbois:** Supervision, Project administration. **K. Hono:** Supervision, Funding acquisition. **Y.K. Takahashi:** Writing – review & editing, Supervision, Data curation.

Declaration of competing interest

The authors declare that they have no known competing financial interests or personal relationships that could have appeared to influence the work reported in this paper.

Acknowledgements

This work was supported by KAKENHI Grants-in-Aid No 23K22803 from the Japan Society for the Promotion of Science (JSPS) and the JST-CREST (JPMJC22C3).

Supplementary materials

Supplementary material associated with this article can be found, in the online version, at doi:10.1016/j.actamat.2025.120743.

References

[1] D. Reinsel, et al., The digitization of the world from edge to core, Framingham: Int. Data Corp. 16 (2018) 1.
[2] V. Özdemir, N. Hekim, Birth of industry 5.0: making sense of big data with artificial intelligence, "the internet of things" and next-generation technology policy, Omics J. Integr. Biol. 22 (2018) 65.
[3] G. Albuquerque, et al., HDD reader technology roadmap to an areal density of 4 Tbpsi and beyond, IEEE Trans. on Magn. 58 (2021) 1.
[4] D. Weller, et al., Review Article: fePt heat assisted magnetic recording media, J. Vac. Sci. Technol. B 34 (2016), 060801-1-10.
[5] K. Hono, et al., Heat-assisted magnetic recording media materials, MRS Bull. 43 (2018) 93–99.
[6] D. Weller, et al., $L1_0$ FePtX–Y media for heat-assisted magnetic recording, Phys. Status Solidi A 210 (2013) 1245–1260.
[7] P. Tozman, et al., Dual-layer FePt-C granular media for multi-level heat-assisted magnetic recording, Acta Mater. 271 (2024), 119869-1-8.
[8] K. Uchida, et al., Observation of the spin Seebeck effect, Nature 455 (2008) 9.
[9] S. Seki, et al., Thermal generation of spin current in an antiferromagnet, Phys. Rev. Lett. 115 (2015), 266601-1-5.
[10] S. Wu, et al., Antiferromagnetic spin Seebeck effect, Phys. Rev. Lett. 116 (2016), 097204-1-5.
[11] I. Gray, et al., Spin Seebeck imaging of spin-torque switching in antiferromagnetic Pt/NiO heterostructures, Phys. Rev. X 9 (2019), 041016-1-10.
[12] S. Rezende, et al., Theory of the spin Seebeck effect in antiferromagnets, Phys. Rev. B 93 (2016) 014425.
[13] R. Umetsu, et al., Magnetic and electrical properties, and mechanism of exchange bias-field of γ-phase and $L1_0$-type antiferromagnetic Mn alloys, Trans. Magn. Soc. Japan 3 (2003) 59.
[14] K. Ogita, et al., Reinvestigation of the magnetic structure in $L1_0$-type MnPt alloy power samples, J. Phys. Soc. Jpn. 79 (2010), 045001-1-2.
[15] C. Xu, et al., Origin of anomalous hysteresis loops induced by femtosecond laser pulses in GdFeCo amorphous films, Appl. Phys. Lett. 96 (2010) 092514.
[16] S. Li, et al., Intrinsic subpicosecond magnetization reversal driven by femtosecond laser pulses in GdFeCo amorphous films, Appl. Phys. Lett. 103 (2013) 242411.
[17] C. Stanciu, et al., At subpicosecond magnetization reversal across ferrimagnetic compensation points, Phys. Rev. Lett. 99 (2007) 217204.
[18] S. Pisana, et al., Measurement of the Curie temperature distribution in FePt granular magnetic media, Appl. Phys. Lett. 104 (2014) 162407.
[19] H.D. Vora, et al., One-dimensional multipulse laser machining of structural alumina: evolution of surface topography, Int. J. Adv. Manuf. Technol. 68 (2013) 6.

[20] S. Iihama, et al., Ultrafast demagnetization of $L1_0$ FePt and FePd ordered alloys, J. Phys. D: Appl. Phys. 49 (2016) 035002.
[21] G.M. Choi, et al., Thermal spin-transfer torque driven by the spin-dependent Seebeck effect in metallic spin-valves, Nat. Phys. 11 (2015) 576.
[22] S. Isogami, et al., Enhancement of spin pumping efficiency in Fe_4N/Pt bilayer films, Appl. Phys. Express 6 (2013) 063004.
[23] S. Isogami, et al., Enhanced inverse spin-Hall voltage in (001) oriented Fe_4N/Pt polycrystalline films without contribution of planar-Hall effect, Jpn. J. Appl. Phys. 55 (2016) 043001.
[24] M. Tsunoda, et al., Uncompensated antiferromagnetic spins at the interface in Mn–Ir based exchange biased bilayers, J. Appl. Phys. 101 (2007) 09E510.
[25] S. Hu, et al., Efficient thermal spin injection using CoFeAl nanowire, NPG Asia Mater. 6 (2014) e127.
[26] S-h.C. Baek, et al., Spin currents and spin–orbit torques in ferromagnetic trilayers, Nature Mater. 17 (2018) 509.
[27] S. Hu, et al., Efficient perpendicular magnetization switching by a magnetic spin Hall effect in a noncollinear antiferromagnet, Nature Commun. 13 (2022) 4447.
[28] A. Slachter, et al., Thermally driven spin injection from a ferromagnet into a non-magnetic metal, Nature Phys. 6 (2010) 879.
[29] K. Uchida, et al., Spin seebeck insulator, Nature Mater. 9 (2010) 894.